

Fast GPU simulation of reinforced concrete at the scale of reinforcement ribs by the discrete element method

R. PACEVIČ^{1,2}), R. KAČIANAUSKAS²), A. KAČENIAUSKAS²),
G. KAKLAUSKAS²), R. BARAUSKAS¹)

¹) *Kaunas University of Technology, Kaunas, Lithuania,*
e-mails: ruslan.pacevic@ktu.lt, rimantas.barauskas@ktu.lt

²) *Vilnius Gediminas Technical University, Vilnius, Lithuania,*
e-mails: ruslan.pacevic@vgtu.lt, rimantas.kacianauskas@vgtu.lt,
arnas.kaceniauskas@vgtu.lt, gintaris.kaklauskas@vgtu.lt

THE PAPER PRESENTS THE DEVELOPMENT OF THE GPU-BASED DISCRETE ELEMENT METHOD (DEM) code for simulating damage and fracture of cohesive solids with application to reinforced concrete at the scale of reinforcement ribs. The solid volume of concrete and steel is modelled by bonded spherical particles. Very fine discretization, containing more than million particles, is applied to describe the 3D reinforcement bar geometry at the scale of ribs and to investigate cracking behaviour of concrete near the reinforcement bar. The numerical model is validated by using experimental results of the double pull-out test. Influence of the discretization scale to the numerical solution is evaluated by using the reinforcement strain profiles and the cracking patterns. The developed GPU-based DEM algorithm efficiently handles interaction of particles, does not require any atomic operation and allows performing fast damage and fracture simulations with large number of particles. The performance measured on GPU is compared with that attained on different CPUs for varying number of particles. The high value of the Cundall number (particle number multiplied by time steps computed per second) equal to $4.3E+07$ is measured on NVIDIA®Tesla™P100 GPU in the case of 1858560 particles.

Key words: discrete element method, bounded particle model, damage and fracture simulation, reinforced concrete, ribbed steel reinforcement, OpenCL, GPGPU.

Copyright © 2019 by IPPT PAN, Warszawa

1. Introduction

THE DISCRETE ELEMENT METHOD (DEM) or so called distinct element method, suggested in pioneering work of CUNDALL and STRACK [1], opened new vistas in modelling of materials. The concept of the DEM presents numerical methodology, providing a quantitative description of discrete particulate media by considering motion and deformation behaviour of individual particles in the frame of Newtonian mechanics. Traditionally, the DEM methodology is related to physical nature of granular materials. The granular microstructure of the material

is modelled as a statistically generated assembly of non-cohesive particles of different shapes and sizes. The proper interactions between particles need to be defined to account for the macroscopic mechanical properties of the medium. Main advantages of the particle-based modelling methodology include the simple mathematical treatment of the problem, whereby complex constitutive relationships are replaced by simple particle contact logic. The main aspects of the theoretical DEM framework, new findings and application samples of granular flows are addressed to selected reviews, see [2–4]. Nowadays DEM is acknowledged to be an effective procedure not limited for analysis of non-cohesive granular materials [5, 6], but extended to cohesive powders [7], fluidized environments [8], rock cutting [9] and couplings with different multiphysics [10–12].

The specific DEM application area is related to damage of heterogeneous multiphase continuum. Practically, most of the main produced engineering materials, including concrete and reinforced concrete, as well as natural minerals fall into this category. The state of damaged concrete with propagating cracks may be regarded as fragmentation of initially stable heterogeneous continuum or assembly of bonded particles characterized by an unstable structure. DEM can take into account most kinds of discontinuities and material failure since the medium is considered as naturally discontinuous. In the case of intensive cracking, DEM is a powerful alternative to the finite element modelling, because it does not rely on any assumption regarding where and how cracks occur and propagate [13].

Many particle- or lattice-based numerical methods for concrete modelling on aggregate scale (mesoscale or microscale) can be classified to an unified approach termed hereafter by the common name Lattice Discrete Particle Method (LDPM). The earliest methods are based on structural networks or lattice discretization techniques. The lattice methods [14] explore a regular grid structure considered on a finer scale than an aggregate size. Theoretical aspects of the relationship between DEM and lattice discretization of continuum are generalized by OSTOJA-STARZEWSKI [15]. According to other approaches, a heterogeneous material is modelled as a web of elements, connecting discrete particles of different materials. Continuity of inhomogeneous solids including concrete can be represented by cohesive particles [16]. A cohesive model for discrete particles combined with experimental data has been demonstrated by NITKA and TEJCHMAN [17]. POTYONDY and CUNDALL [18] have proposed a numerical discrete element model called the bonded particle model (BPM) to simulate the fracture behaviour. The material has been represented by a dense packing of circular or spherical particles bonded at their contact points. Two types of bonds are typically used in BPM: the contact bond and the parallel bond. In the parallel bond model, the moment induced by particle rotation is resisted by a set of elastic springs uniformly distributed over a finite-sized section, ly-

ing on the contact plane and centred at the contact point. This bond model reproduces the physical behaviour of a cement-like substance gluing adjacent particles together. In the contact bond model, an elastic spring with constant normal and shear stiffness acts at the contact points between particles, allowing only forces to be transmitted. The original LDPM elaborated by CUSATIS *et al.* [19] reflects concrete mesostructure by a system of interacting polyhedral aggregate particles connected by a lattice system that is obtained through a Delaunay tetrahedralization of the aggregate centres and the Voronoi tessellation. The mechanical interaction among adjacent aggregate particles is governed by mesoscale constitutive equations, simulating mesoscale tensile fracturing with strain-softening, cohesive and frictional shearing, and nonlinear compressive behaviour with strain-hardening.

Remarkable developments are also related to modelling of reinforced concrete, where different concepts and techniques how to evaluate reinforcement may be found. The earlier discussed LDPM combined with a homogenization procedure on the fine scale has been applied for the macroscopic response analysis of reinforced concrete structures by LALE *et al.* [20]. A specific 3D mesoscale model with discrete fibers for reinforced high strength concrete has been successfully developed and verified by LIANG and WU [21]. A similar model, conducting randomly distributed aggregates, has been suggested by ZHANG *et al.* [22]. REN *et al.* [23] have simulated the tensile and compressive failure process of concrete by using a user-defined BPM based on the modified parallel bond. Stochastic nature of reinforced concrete in lattice models has been illustrated by ZABULIONIS *et al.* [24]. An important issue of reinforced concrete modelling is incorporation of the reinforcement bars and, especially, description of the bond between the concrete and the reinforcement. Continuum formulation of the concrete and the reinforcement interaction is presented by RABCZUK *et al.* [25]. Here, several important issues of modelling reinforced concrete structures are manifested. Firstly, the experimental crack pattern usually cannot be well reproduced. Secondly, bond models can be developed at three different scales, and geometry of the bar surface, comprising the scale of the ribs, have to be considered. The nature of cracking around the bond is comprehensively discussed by RABCZUK and BELYTSCHKO [26] and DESNERCK *et al.* [27]. However, the presented cracking patterns around the bar are rather of a hypothetical character, therefore, novel contributions to modeling of this effect are desirable.

In spite of considerable advances of computer hardware, the simulation of reinforced concrete structures at the discretization level necessary for the reinforcement bar geometry has the disadvantage of making DEM computationally very expensive [28]. Naturally, to solve the industrial-scale problems, parallel computing has become an obvious option for significantly increasing computa-

tional capabilities. However, the selection of the efficient parallel solution algorithm is highly dependable on the specifics of the considered problem and numerical method [28–30]. Today, usage of GPUs as general coprocessors is a major trend in high performance computing, usually called the general purpose GPU (GPGPU). High peak performance associated with moderate cost of GPU makes them good candidates to dramatically boost the performance of the computing node. Some GPUs are dedicated to GPGPU like the NVIDIA Tesla family, and software environments like CUDA [31] or OpenCL [32] are targeted at GPGPU programming. However, efficient GPU codes with implemented practical DEM models for simulation of industrial applications still present challenges.

The main focus and the novelty of the present paper is to evaluate the cracking behaviour of the concrete in the vicinity of the reinforcement bar by applying fine discretization related to the scale of the ribs. To retain natural deformation gradients and to avoid artificial effects, occurring by variable discretization density, the uniform fine discretization with particle diameters smaller than height of ribs is applied for the entire volume of the member. The simulations based on the preferable discretization scale require very large computational resources to solve the described problem in a full scale. The considered DEM model and developed GPU code are employed to solve the problem with reasonable computational resources.

Other parts of the paper are organized as follows: Section 2 presents a discussion on the related works, Section 3 outlines the governing relations of the DEM, Section 4 provides the developed GPU algorithm for damage and the fracture simulation by DEM, Section 5 describes the considered problem, including the experimental double pull-out test of the reinforced concrete prism, Section 6 presents the numerical results and performance analysis, while Section 7 gives the concluding remarks.

2. The related works

The computing time of industrial applications can be significantly reduced exploiting the parallelization benefits of the graphical processing unit (GPU), which is becoming increasingly more important as an alternative computational platform for DEM simulations [5] RADEKE *et al.* [33] have proposed an approach of using CUDA for DEM, which enabled a simulation of more than two million particles per gigabyte of the GPU memory. NISHIURA *et al.* [34] have developed several novel algorithms for a shared memory concurrent computation of particle simulations and measured their efficiency and scalability on various shared memory architectures, including GPUs. YUE *et al.* [35] have made a GPU version of Trubal code and demonstrated its application in die filling. In 3D simula-

tions, containing 20000 particles, an average speed-up of 19.66 has been achieved on NVIDIA Tesla K40c card. GOVENDER *et al.* [5] have simulated the hopper discharge flow with the non-convex polyhedral particles by using the modular high performance Blaze-DEMGPU framework for the GPU architecture. Recently, ZHENG *et al.* [36] have presented a GPU-based DEM-FEM computational framework implemented by CUDA FORTRAN for tire-sand interaction simulations. In general, the simplified DEM models without consideration of rotational components of the contact force or incremental friction model [5, 33] result in a significant speedup on GPU. WASHIZAWA *et al.* [37] have demonstrated that the computing speed of the practical model, considering more forces between interacting particles, is 7 times slower than that of the simplified model on GPU. Thus, efficient GPU codes with implemented complex physical models still present challenges.

To achieve a higher speedup ratio for a larger number of particles, a few efforts have been made to use the combined GPU and MPI technology. The one-dimensional domain decomposition with multiple GPUs has been applied to simulation of 128 million particles by TIAN *et al.* [38]. GAN *et al.* [39] have developed the multiple GPU-based DEM software and modelled the screw conveyor and rotating drums. Simulations of large granular systems with more than 10 million particles have demonstrated that the speed using 32 GPUs can be 18 times faster than a single GPU. However, data transfer from the GPU memory to CPU and communication overhead between nodes leads to a significant decrease of the parallel performance and primitive topology of domain decomposition.

In the case of the damage modelling based on the failure of bonds between particles, a speed-up for the self-compacting concrete flow simulations [40] has been up to 35 with nearly 30000 particles on the GPU card GTX 580 in comparison with the Fortran code, running on one core of 2.93 GHz Intel Core i7 CPU. The complex and costly contact search algorithm, allowing a particle to overlap an arbitrary number of cells [40], has performed well up to 140063 heterogeneous particles in the case of the gravity packing problem. However, the moderate GPU resources have reduced the maximum number of used particles to 29580 in the case of the complex physical model of self-compacting concrete flow. DURAND *et al.* [41] simulated an impact on a reinforced concrete slab on GPU. However, challenging implementation of the fracture model with normal and tangent failure criteria and insufficient GPU resources have also limited the number of used particles to 14274, which is not enough in the case of civil engineering structures. Thus, the efficient GPU algorithm for the complex physical models of damage and fracture leads to challenging implementation on shared memory architectures, and quantitative performance analyses are still of interest in the case of large number of particles.

3. Governing relationships

On macroscopic scale, the reinforced concrete model is considered as two-phase solid body. The elaborated discrete model assumes the volume of the body as a particulate domain composed by the finite number of bonded solid particles. The dynamic behavior of the discrete system is described by considering motion and deformation of interacting individual particles in the frame of Newtonian mechanics. Motion of particles is described in the first subsection, while computation of forces is presented in the second subsection.

3.1. Equations of motion

An arbitrary particle i in the system of N particles is characterized by three translational and three rotational degrees of freedom and undergoes the translational and rotational motion described in time t as follows:

$$(3.1) \quad m_i \frac{d^2 \mathbf{x}_i}{dt^2} = \mathbf{F}_i, \quad I_i \frac{d\boldsymbol{\omega}_i}{dt} = \mathbf{T}_i,$$

where m_i and I_i are the mass and the moment of inertia of the particle i , respectively, while \mathbf{x}_i and $\boldsymbol{\omega}_i$ are the position vector of the particle centre and the rotational velocity around the centre of mass of the particle i . The vectors \mathbf{F}_i and \mathbf{T}_i present the resultant force and the resultant torque, acting in center of the particle i . Formulation and integration of rotational motion slightly differs from that of translational motion. Translational motion is completely defined by the position vector \mathbf{x}_i of the particle centre, velocity vector and acceleration that are defined by integration of the first equation in (3.1). Rotational motion described by angular velocity $\boldsymbol{\omega}_i$ and angular acceleration is valid for spherical particles in 3D. The employed formulation of rotational motion is simplified with respect to a general form for an arbitrary rigid body with the rotational inertial properties represented by a second order tensor. Evaluation of time-dependent orientation of particles defined by three angles presents additional task. For details several references could be recommended [2, 42]. The above equations along with the specified initial conditions present an universal mathematical model, capturing large amount of problems encountered by the DEM and various extensions. This rather standard DEM model has been described in countless review papers and problem-oriented applications, therefore, only the most important aspects will be outlined hereafter.

The proper formulation of the considered problem is governed by the right-hand forces. These forces may depend on the base of subject-related physical nature, modelling approach and many other factors. The vector \mathbf{F}_i can be expressed by the external force and sum of the contact forces between interacting

particles that are indicated by subscript $j = 1, N_c$:

$$(3.2) \quad \mathbf{F}_i = \mathbf{F}_{i,ext} + \mathbf{F}_{i,cont} = \mathbf{F}_{i,ext} + \sum_{j=1, j \neq i}^{N_c} \mathbf{F}_{ij,cont},$$

where $\mathbf{F}_{i,ext}$ and $\mathbf{F}_{i,cont}$ are the external force and the resultant contact force of particle i , respectively, $\mathbf{F}_{ij,cont}$ is the interparticle contact force vector, describing the contact between the particles i and j . In the present research, the electromagnetic force [43], the aerodynamic force [44] and other external forces [45], including the gravity force are not considered. The rotational motion is governed by particle torques \mathbf{T}_i that can be expressed by torques \mathbf{T}_{ij} of neighboring particles:

$$(3.3) \quad \mathbf{T}_i = \sum_{j=1, j \neq i}^{N_c} \mathbf{T}_{ij} = \sum_{j=1, j \neq i}^{N_c} \mathbf{d}_{cij} \times \mathbf{F}_{ij,cont},$$

where \mathbf{d}_{cij} is the vector pointing from the particle centre to the contact centre. The interparticle contact force vector $\mathbf{F}_{ij,cont}$ may be expressed in terms of normal and tangential components.

$$(3.4) \quad \mathbf{F}_{ij,cont} = \mathbf{F}_{ij,n} + \mathbf{F}_{ij,t} = F_{ij,cont,n} \mathbf{n}_{ij} + F_{ij,cont,t} \mathbf{t}_{ij},$$

where \mathbf{n}_{ij} is the unit normal vector, \mathbf{t}_{ij} is the unit vector of the tangential contact direction.

3.2. Computation of forces

DEM is well adopted to simulate a granular media with repulsive interaction, but the description of solid is more challenging. Generally, 3D heterogeneous continuum may be presented as 3D box fulfilled by particles embedded into material substance like cement. Several models for computation of cohesive interparticle forces dependent on the properties and geometry may be found in practical use [13–18]. Probably, the mostly detailed approach earlier termed as a bonded particle model was elaborated by POTYONDY and CUNDALL [18]. According to the BPM, the interaction of the particles can be defined by a connection element, which reproduces the physical behaviour a cement-like substance gluing adjacent particles together. In the present research, heterogeneity is defined in a fine scale, and packing of particles is dense. Since the interparticle bond length is negligibly small, contribution of the bond can be neglected. This simplification presents a particular case of BPM, termed by authors of [18] as the contact bond. Assuming the linear relationship with the displacement $\boldsymbol{\delta}_{ij}$, the contact force can be expressed:

$$(3.5) \quad \mathbf{F}_{ij,cont} = K_{ij} \boldsymbol{\delta}_{ij}.$$

The resultant stiffness of the connecting element K_{ij} can be expressed by stiffness parameters of contacting particles K_i and k_j :

$$(3.6) \quad K_{ij} = \frac{k_i k_j}{k_i + k_j}.$$

Generally, interaction of particles via interface material presents 3D continuum problem. A detailed FEM analysis of this contact has been performed by ZANG and WONG [46] and PILKAVIČIUS *et al.* [47]. Results have shown evidence that bond stiffness depends on microproperties of material and radiuses of interacting particles and simplified expressions are not accurate. Therefore, calibration of microconstants is often performed [4, 48].

According to a linear contact model, the normal force is computed according to formula [2]:

$$(3.7) \quad \mathbf{F}_{ij,n} = \frac{4}{3} \frac{E_i E_j}{E_i(1 - \nu_j^2) + E_j(1 - \nu_i^2)} R_{ij} \delta_{n,ij} \mathbf{n}_{ij},$$

where R_{ij} is the reduced radius of two particles, E_i and E_j are elastic moduli, ν_i and ν_j are Poisson's ratios of the spherical particles i and j , respectively. The depth of the overlap between particles i and j is defined by $\delta_{n,ij}$. In the present research, the viscous energy dissipation is not considered. The tangential contact force is computed by summing the elastic components of the spring model [2, 49]:

$$(3.8) \quad \mathbf{F}_{ij,t} = -\frac{16}{3} \cdot \frac{G_i G_j \sqrt{R_{ij} \delta_{n,ij}}}{G_i(2 - \nu_j) + G_j(2 - \nu_i)} |\delta_{t,ij}| \mathbf{t}_{ij},$$

where $|\delta_{t,ij}|$ is the length of tangential displacement $\delta_{t,ij}$, G_i and G_j are shear moduli of the particles i and j , respectively. The unit vector \mathbf{t}_{ij} of the tangential contact direction can be obtained according to formula:

$$(3.9) \quad \begin{cases} \frac{\mathbf{v}_{t,ij}}{|\mathbf{v}_{t,ij}|}, & \nu \neq 0, \\ \frac{\delta_{t,ij}}{\delta_{t,ij}}, & \nu_{t,ij} = 0, \delta_{t,ij} \neq 0, \\ 0, & \text{otherwise.} \end{cases}$$

where $\mathbf{v}_{t,ij}$ is the tangential component of the relative velocity of the contact point. The vector of tangential displacement is obtained from the temporal integration of the tangential component of the relative velocity $\mathbf{v}_{t,ij}$, starting at the time instant when particles i and j came into contact:

$$(3.10) \quad \delta_{t,ij}(t_C) = \int_{t_0}^{t_0+t_C} \mathbf{v}_{t,ij}(t) dt = \sum_{i=1}^{i_C} \mathbf{v}_{t,ij}(t_0 + i\Delta t) \Delta t,$$

where T_C denotes either the end time of the contact or the current time. The approximate time integration is performed by using an incremental approach. At each time step, the current value of the tangential component of the relative velocity is multiplied by the time step value and added to the accumulated result of the previous time steps, which should be saved at each time step of the contact. Thus, tangential force-displacement behavior is simplified in such a manner, where a stepwise solution is available without memorizing the whole loading history [50]. The details of model application can be found in [51].

The implemented contact bonds can break when the external loading exceeds the strength of bonds, leading to crack formation directly between two particles. The bonds are broken instantaneously, when the bond strength is exceeded in the normal direction by the tensile contact force or in the tangential direction by the tangential contact force. This process shows fragmentation behaviour of the considered material. The failure criteria can be written as:

$$(3.11) \quad F_{ij,cont,n} \leq R_n,$$

$$(3.12) \quad |F_{ij,cont,t}| \leq R_t,$$

where R_n and R_t are the bond strengths in the normal direction and in the tangential direction, respectively.

If new contacts between particles occur after breakage of bonds, normal and tangential contact forces are computed, using the linear contact model (3.7) and (3.8). A frictional interaction can occur among the particles in the case of recompression. The tangential force is evaluated, assuming the Coulomb model of friction:

$$(3.13) \quad \mathbf{F}_{ij,t} = -t_{ij}\mu|\mathbf{F}_{ij,n}|,$$

where μ is the Coulomb friction coefficient. The force-displacement relationships for the normal and tangential contact interaction in the elastic perfectly brittle model are shown in Fig. 1.

Figure 2 shows the force-displacement relationships for the elastic-softening constitutive model [7, 9], which is considered as an alternative contact model; δ_n^{crit} and δ_t^{crit} are the critical values of the normal and tangential relative displacements. The softening slopes can be defined by the softening parameters c_n^{soft} and c_t^{soft} in the normal and tangential directions, respectively.

The applied method can simulate the motion of individual particles and also the behaviour of bulk material formed by assembling many particles through bonds at contacts. It is worth noting that the priority of modelling strategy is to achieve required accuracy with the simplest computational models by increasing the number of particles in the case of the fast DEM simulation on GPU.

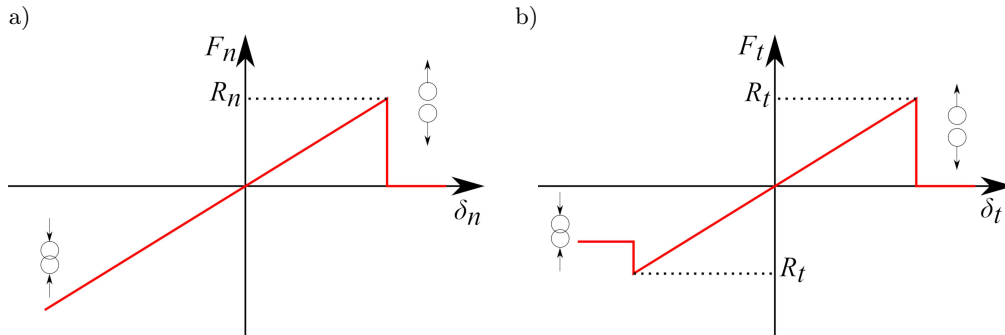


FIG. 1. Force-displacement relationships for the elastic perfectly brittle constitutive model: a) in the normal direction; b) in the tangential direction.

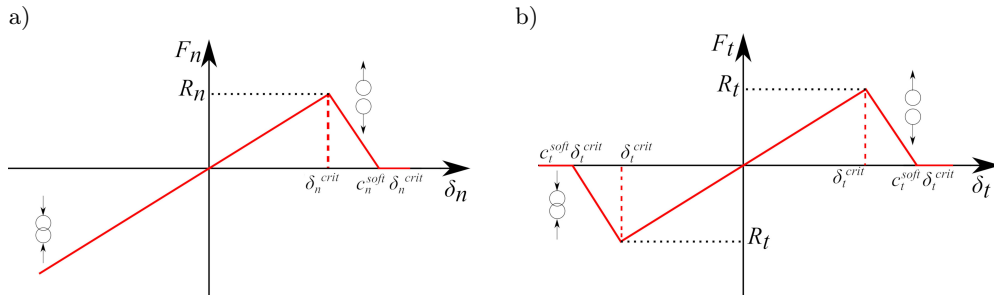


FIG. 2. Force-displacement relationships for the elastic-softening constitutive model: a) in the normal direction; b) in the tangential direction.

4. The developed DEM algorithm for GPU

The GPU-based algorithm is developed by using OpenCL [32] to run the same DEM code on all shared memory architectures, including GPU and CPU of different vendors. In general, contact detection, computation of forces and time integration are the most time consuming parts of double precision DEM computations. In the case of considered damage problems, contact detection can be performed very seldom because of relatively small changes of system topology after interparticle fracture. Moreover, in the case of monosized particles, the simple and fast implementation of a uniform grid algorithm [37] can be used instead of the complex and costly contact search algorithms [40]. Thus, contact detection is not the most time consuming and the most important in the present research. The fifth order Gear predictor-corrector algorithm [51] is used for accurate time integration, which requires more than one GPU kernel for implementation. In the case of damage simulations, the computation of forces is

performed in different ways, depending on the presence and state of the bond between contacting particles. Thus, implementation of the computation of forces is the most challenging because of the fracture model with failure criteria.

The flowchart of the developed GPU algorithm for DEM computations is presented in Fig. 3. At the start of the simulation, preprocessing is performed on CPU and initial data is copied into the GPU memory. No further memory transactions between the CPU and GPU memory is required except the result storage. *Kernel 1* starts the time integration, performing Gear predictor on the thread per particle basis. The new values of displacements, velocities and accelerations of particles are predicted at the time increment by a simple series expansion up to the fifth order of accuracy in this kernel.

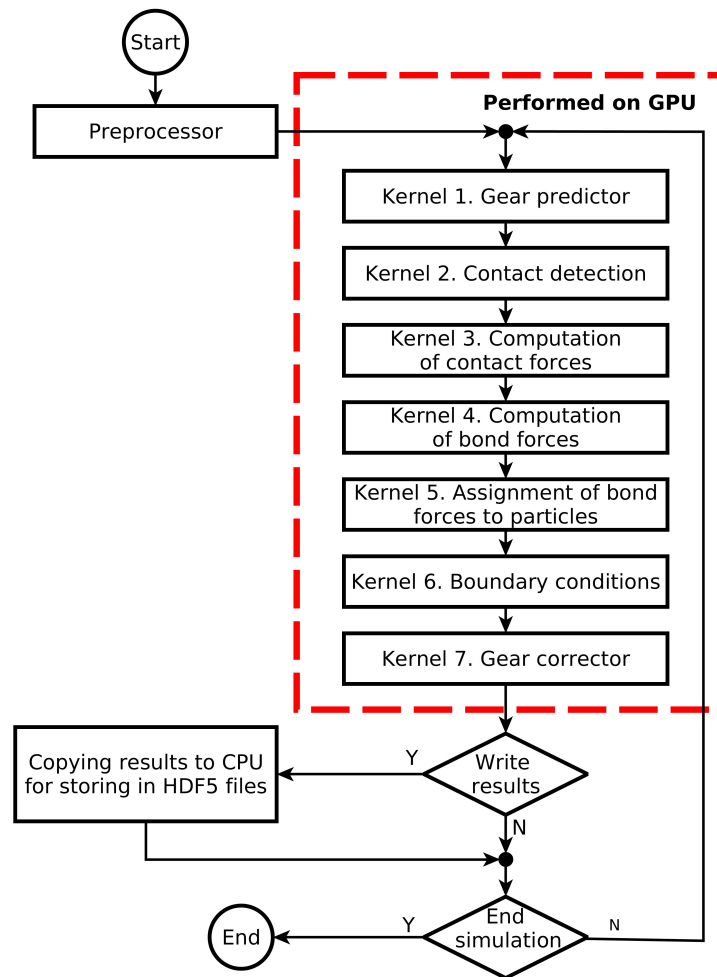


FIG. 3. The flowchart of the developed GPU algorithm.

Kernel 2 performs the contact detection on the thread per particle basis. The simple and fast version of an uniform grid algorithm is implemented to save the computing time in the case of monosized particles. Each particle is assigned to only one cell of the uniform grid based on a position of the particle centre. The size of a grid cell is equal to the particle diameter. The employed kernel stores two arrays containing the list of pairs: cell hash and particle id. Ids of particles are sorted according to their hash values, representing the grid cell. The sorting is performed by using the fast radix sort method. Finally, for each particle, the grid cell, where it belongs, is obtained and contacting particles are searched in a loop through the neighbouring grid cells. When the distance between particles is smaller than the sum of radii of particles, the collision is identified.

Kernel 3 computes contact forces between all overlapped particles ($\delta_{n,ij} > 0$) as in conventional DEM codes for granular flow simulations. All computations are performed by thread per particle, which can be considered as the most convenient and efficient parallelism in the case of DEM computations on GPU. *Kernel 4* computes pulling forces between bonded particles. This kernel works on the thread per bond basis, which is very natural for damage and fracture simulations. The normal and tangential failure criteria (3.11) and (3.12) of bonds are also checked and the bond state array is updated if the bond is broken. The computed values of bond forces are temporally stored in the special purpose arrays to avoid the conflicts of memory access when threads of different bonds writes forces into memory of the same particle at the same time. Thus, atomic operations are avoided and high parallel performance is ensured at the cost of increased memory usage. In the present research, it is assumed that initially determined topology of bonds is fixed and new bonds cannot appear during computations. The developed algorithm exploits this assumption to minimize the increased memory usage. The exact size of additional arrays can be determined according to the list of bonds at the beginning of computations even in preprocessor. The necessary arrays of a minimal size are allocated in the GPU memory before the time loop and their size does not change until the end of computations. This is the main advantage of the developed algorithm over the other DEM algorithms [40, 41] proposed for damage simulations on GPU. In the opposite to the GPU algorithm proposed by DURAND *et al.* [41], the same kernel handles bonds between different types of particles (steel and concrete), which does not reduce the data parallelism.

Kernel 5 assigns the contact forces computed by the previous kernel to particles. It sums values of forces, computed on bonds attached to the processed particle and stored in the special purpose arrays. Thus, it finishes the algorithm started by a previous kernel and stores the computed forces, acting on particles, in memory. This kernel works on the thread per particle basis, avoiding a concurrent memory access, in the opposite to the kernels, performing force computation on the thread per bond basis.

Kernel 6 sets boundary conditions. The symmetry boundary conditions are defined by setting the normal components of displacements of particles located on symmetry planes. Tension is applied by setting velocity values of the certain particles. *Kernel 7* finishes the time integration, performing Gear corrector on the thread per particle basis. The values of displacements, velocities and accelerations of particles are corrected in this kernel. At the end of time step, the particle data can be copied from GPU memory to CPU and stored on a hard disk drive in HDF5 format. It is recommended to transfer the data to CPU memory as seldom as possible because it is a time-consuming process. In the case of 1089892 particles, the result transfer of one time step to CPU memory takes about 0.119 s, which 4.6 times exceeds the computing time of one time step. In the present research, the results are transferred and stored for every 2000 time steps that the transfer time can be neglected.

In the case of DEM application to discretization of solids, computation of forces and time integration are the most time consuming parts of DEM computations, because contact detection can be rarely performed. The time integration performed by *Kernel 1* and *Kernel 7* consumes 14% of the total computing time of 1089892 particles. The computation of contact forces performed by *Kernel 3* takes up to 38% of the total computing time. The computation of bond forces performed by *Kernel 4* and assignment them to particles performed by *Kernel 5* consumes 24% and 19% of the total time, respectively. *Kernel 6* responsible for setting boundary conditions takes 5% of the total time. The execution time of *Kernel 2*, performing rare contact detection, is less than 1% of the total computing time, therefore, can be treated as negligible during the initial phases of damage.

In the case of damage and fracture simulations, the additional operations, such a checking failure criteria, should be performed on bonds between particles, comparing with granular flow computations. Two additional kernels (*Kernel 4* and *Kernel 5*) are employed to perform required computations in the present algorithm. Moreover, maintaining the data arrays employed for bond information handling and efficient force processing increased the used memory up to 31% of the memory required for granular flow computations of the same number of particles. The efficient memory management makes the developed algorithm different from the DEM algorithms proposed by other researchers [40, 41] for damage and fracture simulations. The developed algorithm does not require any atomic operation and allows performing efficient damage simulations with millions of particles.

5. A description of the considered uniaxial tension problem

The load bearing capacity of reinforced concrete structures highly depend on the bond between reinforcing bars and the surrounding concrete. It was already

shown that destruction of the bond by intensive cracking of weaker concrete occurred in the vicinity of the bar. On the other hand, cracking is initiated on a very small scale of bar profile geometry. The uniaxial tension of reinforced concrete member or double pull-out test is considered to illustrate damage of the member. The evidence of the problem nature and the experimental set-up is described in the first subsection while development of the DEM model is presented in the second subsection.

5.1. Experimental measurements

A double pull-out test with recorded strains of the reinforcement bar embedded into the concrete is considered. The performed experiment is an alternative approach to the standard pull-out test, which is the most common experimental technique to study the interaction between reinforcement and concrete. From a measured load-displacement relationship, mean bond stress distribution within the anchorage length as a function of slip (or relative displacement) may be obtained in the standard pull-out test. However, in such a way established bond stress-slip relationship may not be suitable for accurate simulation of tensile and bending members at the serviceability limit state (cracking and deformation analysis). Two main reasons for that are the non-uniform bond stress distribution within the anchorage length and the compressive stress fields in the concrete arising from the supports [53]. In the double pull-out test, bond stress-slip behaviour is obtained from the reinforcement strain curves. This technique does not have the earlier mentioned drawbacks as the concrete stresses are tensile and the bond stress variation can be established throughout the anchorage length instead of taking the averaged bond stress value. The double pull-out test can be performed on short members that have not open cracks or relatively longer specimens that contain one or more open cracks [54]. Short members are preferred, if the objective is deriving a bond-stress relationship as the emerging cracks might significantly complicate the shape of bond stress distribution within the length of the member. Moreover, defining the reference section with zero slip can be rather tricky in the cracked members.

Reinforced concrete prisms of $150 \times 150 \times 270$ mm with 20 mm diameter reinforcing bars instrumented with internal strain gauges were tested. Strain gauges were spaced at 30 mm intervals, allowing to measure strain at 11 points along the bar. The reinforcement was longitudinally cut and glued after placing strain gauges and required wiring inside the bar. The experimental setup, including the geometrical characteristics and the positions of strain gauges and the tested specimen fixed in press, is shown in Fig. 4. Prior to testing, the compressive strength of concrete was determined from cubes ($150 \times 150 \times 150$ mm) and cylinders (150 mm diameter, 300 mm height), which resulted in compressive

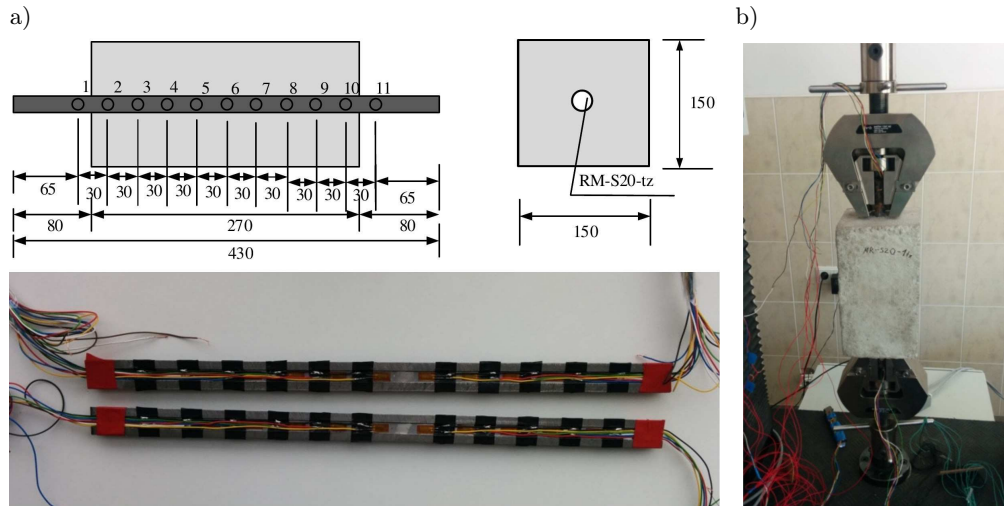


FIG. 4. An experimental setup: a) geometrical characteristics and the positions of strain gauges of the specimen; b) specimen fixed in press.

strength values equal to 45.4 MPa and 40.4 MPa, respectively. The measured elasticity modulus of steel reinforcement was equal to 203 GPa, while that of concrete was equal to 35.6 GPa. Specimens were tested 28 days after casting by using hydraulic machine with displacement control. The load capacity of the machine (200 kN) allowed achieving the maximal strain in the reinforcement of 120 N/m.

The reinforcement strain profile was measured allowing for straightforward calculation of interface zone stresses and slip at any point of reinforcement. It is worth noting that good agreement among independent measurements was obtained. This supposes that accidental experimental errors were minimized and present data may be used to evaluate the adequacy of different numerical modelling techniques. The detailed description of the experimental program, performed at Vilnius Gediminas Technical University in 2016, is given in [55].

5.2. Solution domain and numerical details

Discussion on the DEM model and demonstration the model features is the key issue of recent investigation. As mentioned in previous sections, this study applies to illustrate the numerical DEM technique able to describe failure of the bond. Formally, development of DEM model and spatial discretization of the double pull-out problem by using spherical particles is rather routine task. Due to the axial symmetry, only the 1/8 part of the reinforced concrete specimen shown in Fig. 4 is considered. Geometry of the solution domain is presented in

Fig. 5. Thus, the dimensions of the considered solution domain, containing 12 ribs, are equal to $75 \times 75 \times 138$ mm. The radius of reinforcing bar is equal to 10 mm. The simplified reinforcing bar profile with the assumed height, pitch and width of ribs is also shown in Fig. 5a. This profile is the main characteristic of the bar roughness. The interface surface between concrete and the reinforcing steel bar is obtained by rotating the bar profile about the y axis. Material properties of steel are assigned to particles, which centres are located on the inner side of the interface surface, while other particles are labelled as being concrete particles. In spite of the considered geometric simplifications, the interface surface between concrete and the reinforcing bar formed by ribs has a complicated shape. It is obvious, that singularities of interface might lead to local concentration of stresses and, finally, to local damage occurring on a small scale. Thus, sufficiently fine discretization is necessary to accurately describe the fracture pattern, which leads to high numbers of particles.

The solution domain is discretized by monosized spherical particles that are uniformly distributed by using cubic close pack algorithm, disregarding material properties. Heterogeneity of concrete is considered by defining five fractions of concrete particles with different values of elasticity modulus and bond strengths. The values of elasticity modulus of five fractions are freely selected to preserve the considered value of their harmonic mean according to the homogenization methodology [48]. Thus, it is assumed that heterogeneity of material can be approximated by monosized particles with randomly distributed material properties in the case of sufficiently large number of particles.

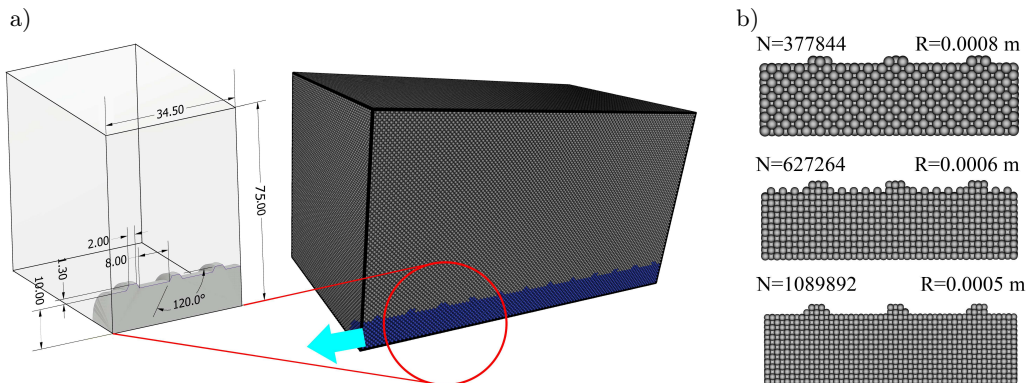


FIG. 5. Discrete model of reinforced concrete under uniaxial tension: a) geometry of the solution domain; b) spatial discretization by using spherical particles.

Different boundary conditions are specified on the domain boundaries. Particles located at the end of steel reinforcing bar are moved with a prescribed constant velocity in y direction, which simulates the uniaxial tension. Displace-

ments and velocities of concrete particles located on the same plane are not fixed. The symmetry boundary conditions are defined on the opposite plane, setting the displacement of concrete and steel particles to zero in y direction. The normal components of displacements of particles are also fixed on the other two symmetry planes crossing each other on the y axis. Figure 5b shows the most often used discretization, consisting of 627264 particles with the radius of 0.6 mm and 3691410 bonds. The comparatively rough discretization consists of 377844 particles with the radius of 0.8 mm, while fine discretization consists of 1089892 particles with the radius of 0.5 mm. It is obvious that highly efficient parallel code is necessary to model damage and fracture of reinforced concrete, simulating behaviour of million discrete particles in a reasonable time.

6. The results

The problem of uniaxial tension of reinforced concrete is considered to examine the performance of the developed GPU algorithm and to validate the applied DEM model. All double-precision computations are performed on the NVIDIA®Tesla™P100 GPU Computing Accelerator (56 Streaming Multiprocessors, 1792 FP64 CUDA Cores, 12GB HBM2, 540GB/s memory bandwidth). Hardware characteristics of the workstation used for quantitative comparison of parallel performance are listed below: Intel®Xeon™E5-2630 2.20GHz 2xCPU, 32GB DDR4 2133MHz RAM. Hardware characteristics of the PC also employed for comparison reasons are listed below: Intel®Core™i7-6700 3.40GHz CPU, 32GB DDR4 2133MHz RAM. Preprocessing, visualization and computations are performed on the computational infrastructure of Vilnius Gediminas Technical University, hosting software services [52] for the DEM simulations.

6.1. Performance analysis

The actual computation time spent on 100000 time steps is measured to investigate the computational efficiency of the developed code for damage and fracture simulations in the case of different numbers of particles; 7 assemblies of monosized particles are generated to represent the reinforced concrete prism. The numbers of particles are 29040, 42500, 67280, 117600, 377844, 627264, 1089892 and 1858560.

Figure 6 shows the scaling performance of the developed GPU code, increasing the number of particles. The curves GPU-P100, CPU-E5-2630 and CPU-i7-6700 represent an average execution time per time step measured on NVIDIA®Tesla™P100, Intel®Xeon™E5-2630 and Intel®Core™i7-6700, respectively. It can be observed that the computational time rises linearly with the

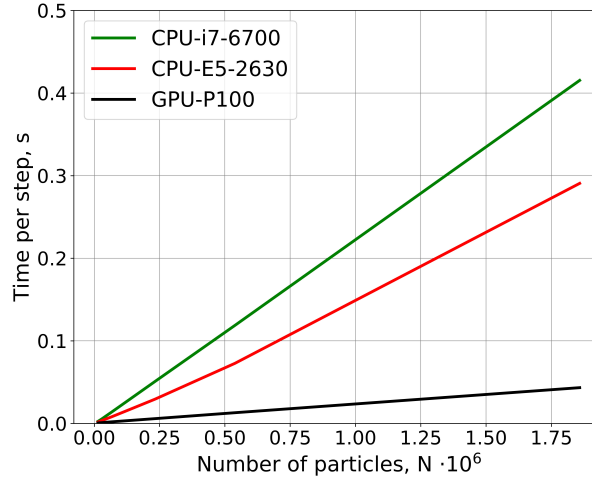


FIG. 6. Performance scaling with number of particles.

increase of particle number, which demonstrates the scalability of the developed parallel DEM algorithm.

The same OpenCL code optimized for multithread shared memory architectures is executed on Intel®Xeon™E5-2630 CPU and Intel®Core™i7-6700 CPU to evaluate the speedup ratio of GPU to CPU. In the case of Intel®Core™i7-6700 CPU with 4 physical cores, the measured speedup values varies from 3.93 to 9.58 for different numbers of particles. In the case of more powerful Intel®Xeon™E5-2630 CPU with 20 physical cores, the lower speedup values, varying from 2.71 to 6.71, are measured. Higher differences become obvious in the case of larger numbers of particles. The sufficiently high speedup values can be observed in spite of intensive usage of advanced vector extensions by OpenCL on CPU and comparatively powerful Intel®Xeon™E5-2630 CPU employed for the comparison.

In absolute values, the developed code computes 23.1 time steps/frames per second (FPS) in case of 1858560 particles, which leads to the Cundall number (FPS \times number of particles) $C = 4.3E+07$. The direct comparison with performance achieved by other authors can be hardly performed because of different physical models implemented, different particle systems used and different hardware employed in different research. However, the measured performance is higher than that (C varies from $6.0E+05$ to $2.2E+06$) obtained with GPU implementation of BPM for concrete by ZHENG *et al.* [40], because of a larger number of particles. Moreover, the achieved performance is comparable with the results of various authors [5, 33, 35, 39] in spite of simpler DEM models without damage simulation implemented and tested on GPU.

6.2. Reinforced concrete simulations

Damage of the reinforced concrete prism is simulated by using the developed GPU code to validate the considered DEM model. The elastic perfectly brittle constitutive model (Fig. 1) is used in the most of computations. A plastic range during shearing is not considered, because the load does not reach it in the simulated experiment. Calibration of the DEM model is performed by using results of the experimental tests [55]. The values of the elasticity modulus of steel particles are calibrated according to the load-displacement curve of the reinforcement bar shown in Fig. 7. The curve is obtained from experimentally measured elasticity modulus of steel reinforcement equal to 203 GPa. Elasticity moduli of steel particles equal to 1250 GPa, 1300 GPa and 1400 GPa are obtained from calibration results in the case of particles with the radii of 0.5 mm, 0.6 mm and 0.8 mm, respectively. Poisson's ratio of steel particles is assumed to be equal to 0.3.

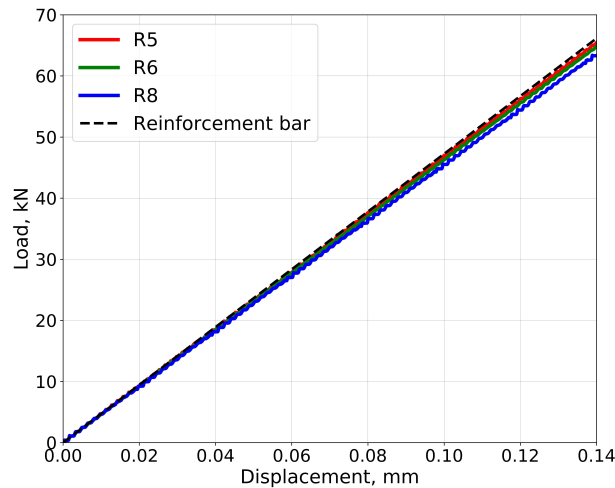


FIG. 7. The load-displacement curve of the reinforcement bar.

The elasticity moduli of the concrete particles is calibrated according to the strain curve of the load equal to 22 kN (Fig. 8). Heterogeneity of concrete is modelled by defining five fractions of concrete particles with different values of elasticity modulus and bond strength, preserving the harmonic mean values of the considered material properties. In the case of the rough discretization model, consisting of 377844 particles with the radius of 0.8 mm, the values of elasticity modulus of five concrete fractions vary from 60 GPa to 80 GPa with the harmonic mean equal to 70 GPa. In the case of 627264 particles with the radius of 0.6 mm, the values of elasticity modulus of concrete fractions vary from 50 GPa to 80 GPa

with the harmonic mean equal to 60 GPa. In the case of 1089892 particles with the radius of 0.5 mm, the values of elasticity modulus of concrete fractions vary from 44 GPa to 70 GPa with the harmonic mean equal to 57 GPa. Poisson's ratio of concrete particles is considered to be equal to 0.2, while the friction coefficient is assumed to be equal to 0.5 in the case of all discretization models.

In the normal direction, the bond strength values of five concrete fractions of the rough model, consisting of 377844 particles with the radius of 0.8 mm, is assumed to vary from 9.0 N to 10.0 N with the harmonic mean equal to 9.5 N. In the case of 627264 particles with the radius of 0.6 mm, the normal bond strength values of concrete fractions vary from 7.0 N to 8.0 N with the harmonic mean equal to 7.5 N. In the case of 1089892 particles with the radius of 0.5 mm, the normal bond strength values of concrete fractions vary from 5.0 N to 6.0 N with the harmonic mean equal to 5.5 N. In the tangential direction, the bond strength values are obtained multiplying the normal bond strength by the coefficient equal 0.2 for all discretization models.

Figure 8 shows the quantitative comparison of numerical results with the experimental measurements. Figure 8a presents reinforcement strain profiles obtained from the experimental double pull-out test for different load values and those extracted from DEM computations with different radii of particles. Figure 8b presents load-displacement curves obtained from experimentally measured strain profiles by means of numerical integration and those obtained from DEM computations with different radii of particles. In Fig. 8a, a set of curves "Experiment" represents the strain profiles of reinforced concrete obtained from experimental measurements for different load values. In Fig. 8b, curves "Experiment" and "Reinforcement bar" represent the load-displacement of reinforced concrete member and reinforcement bar without concrete, respectively. The sets of curves "R5", "R6" and "R8" represent the strain profiles and load-displacement curves computed numerically by using 1089892, 627264 and 377844 particles, respectively. Thus, the influence of the number of used particles on the accuracy of DEM solution can be also evaluated.

The values of the parameters of the DEM model are calibrated according the strain curve of the load equal to 22 kN. Thus, the accurate solution is obtained in the case of the load equal to 34 kN. In Fig. 8a, larger differences between DEM solution and experimental measurements can be observed for larger load values. The numerical results are accurate enough at the end of the reinforced concrete prism in all cases. In the case of 1089892 particles with radius $R = 0.5$ mm, the numerical error varies from 0.2% to 3.4% of the experimentally measured strain for different load values. Significant errors can be observed at the mid-section of the specimen because of the difficulties related with the considered symmetry boundary conditions and the calculation of strains from the discrete model. In the case of 377844 particles with radius $R = 0.8$ mm, the numerical

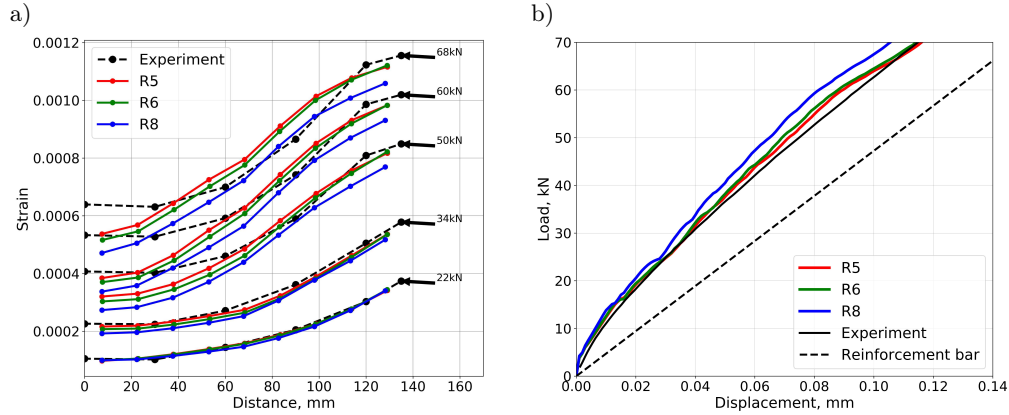


FIG. 8. Comparison of numerical results with the experimental measurements: a) strain dependency on the distance from midsection for different load values; b) load-displacement curves with different radii of particles.

error varies from 4.6% to 36.4% of the experimentally measured strain for different load values. The most accurate results are obtained performing simulations with the largest number of particles equal to 1089892 (radius $R = 0.5$ mm). The differences between the strain curves extracted from simulations with 1089892 and 627264 particles are not large. It is worth noting that the solution obtained by using the smallest set of 377844 particles with the radius of 0.8 mm is not enough accurate, especially, for larger load values. The averaged numerical error reaches 14.9% of the experimentally measured strain in the case of the load equal to 60 kN. The same tendency can be observed in the case of load displacement curves (Fig. 8b). The load-displacement curves extracted from simulations with 1089892 and 627264 particles are in good agreement with experimental measurements. However, the load displacement curve “R8” obtained from simulations with 377844 particles with the radius of 0.8 mm is less accurate. Thus, the discrete model of 627264 particles with the radius of 0.6 mm is considered as the reference model for further simulations to obtain a sufficiently accurate solution in a reasonable computing time.

Figures 9 and 10 show formation and propagation of cracks in the reinforced concrete prism simulated by using 627264 particles. Cracks are visualized by using the local Voronoi decompositions generated according to the topology of bonds and the positions of the neighbouring particles [52]. The local decompositions are generated in the vicinity of broken bonds that are mapped on the Voronoi faces between the bonded particles. Finally, the Voronoi faces are described by graphics primitives, coloured in red and rendered. Thus, the two-dimensional surfaces of propagating cracks can be constructed from broken

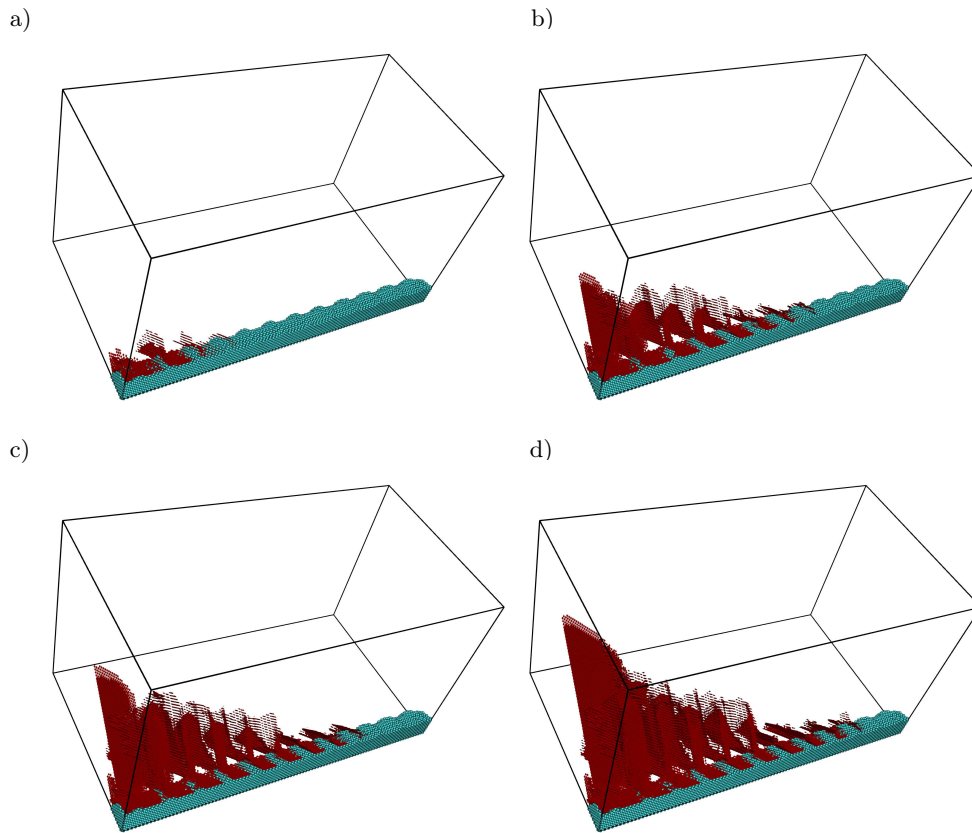


FIG. 9. Crack propagation in the reinforced concrete prism: a) $t = 0.004$ s; b) $t = 0.008$ s; c) $t = 0.010$ s; d) $t = 0.012$ s.

one-dimensional bonds between the neighbouring particles. The algorithm of the local Voronoi-based technique is implemented in the visualization engine of cloud visualization software service VisLT [52].

It can be observed that initial damages of concrete form in front of the ribs of steel reinforcement (Fig. 9a). The first damages form near the steel ribs located at the moving end of the reinforcement while the next damages form at the sequent ribs in the direction of the midsection of the specimen. Later the radial crack forms at the moving end of the reinforcement and propagates towards the midsection of the specimen, which can fracture the reinforced concrete member at higher load. Figure 10 shows radial crack at the end of the reinforced concrete member, which is observed performing the double pull-out test (Fig. 10a) and obtained numerically (Fig. 10b). DEM computations qualitatively capture the formation of the radial crack at the end of the reinforced concrete member.

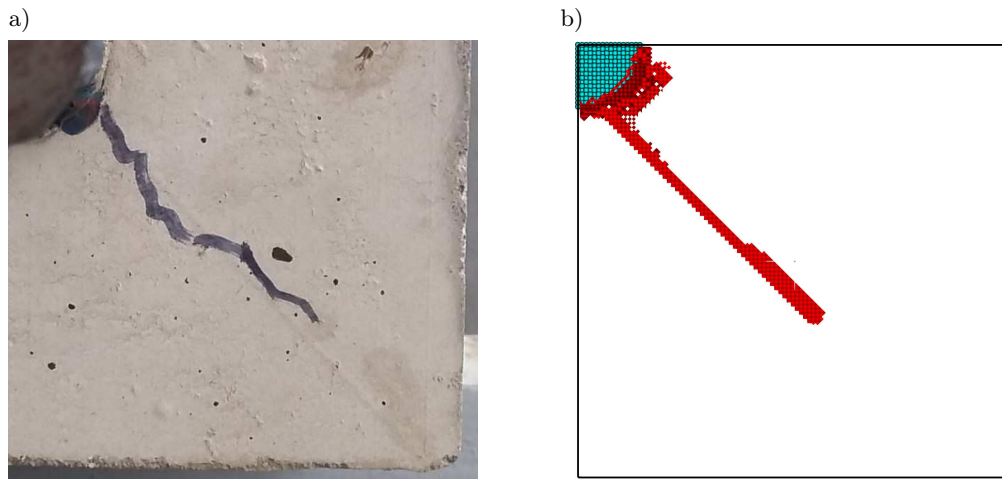


FIG. 10. Radial cracks at the end of the reinforced concrete member: a) the experiment; b) DEM computations.

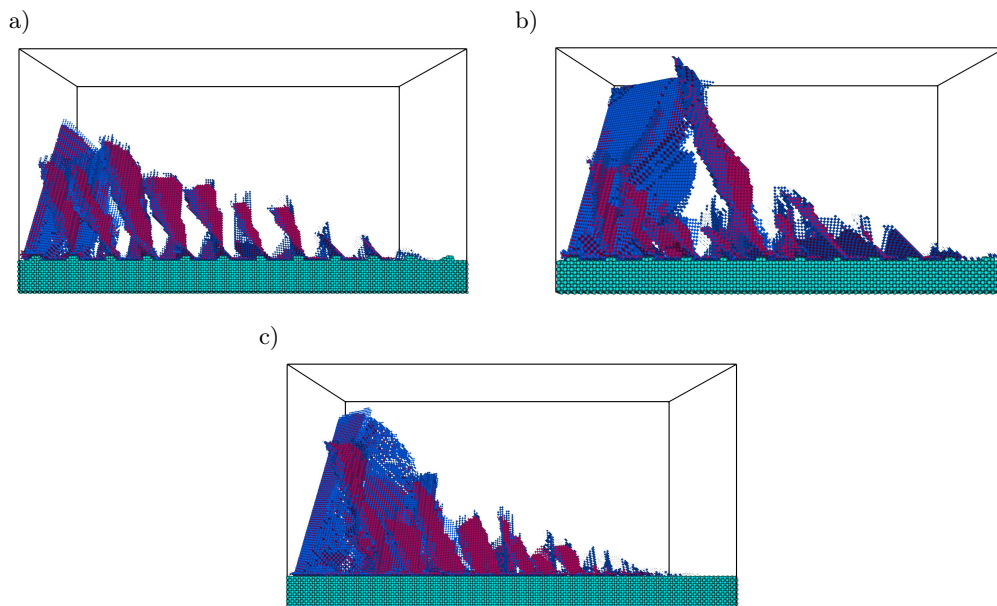


FIG. 11. The effect of the reinforcement bar roughness: a) the reinforcement bar with ribs ($R = 0.5$ mm); b) the reinforcement bar with ribs ($R = 0.8$ mm); c) the reinforcement bar without ribs ($R = 0.5$ mm).

Figure 11 shows the effect of reinforcement bar roughness on crack patterns. Cracks caused by bond breakage according to the normal failure criterion (3.11) are coloured in red, while cracks caused by bond breakage according to the tan-

genial failure criterion (3.12) are coloured in blue. Figures 11a and 11b show the reinforcement bar represented by particles with the radii of 0.5 mm and 0.8 mm, respectively. It can be observed that the crack pattern obtained by using small particles with the radius of 0.5 mm is more regular than that computed by using rough discretization based on large particles with the radius of 0.8 mm. Moreover, the radial crack obtained by using the rough discretization is significantly larger, which is in agreement with the load-displacement curves in Fig. 8b. Thus, discretization scale has a significant influence on the crack pattern. Figure 11c shows the reinforcement bar without ribs discretized by small particles with the radius of 0.5mm. The crack pattern is also less regular than that presented in Fig. 11a, which is in agreement with conclusions made by RABCZUK *et al.* [25]. It also can be observed that larger radial crack is obtained in the case of the reinforcement bar without ribs.

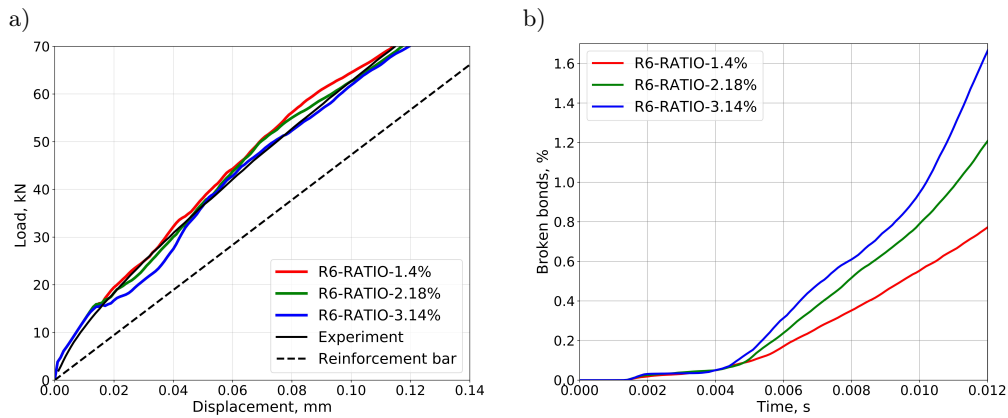


FIG. 12. The effect of reinforcement ratio: a) the load-displacement curves; b) the percentage of broken bonds.

Figure 12 shows the effect of reinforcement ratio on load-displacement curves (Fig. 12a) and the percentage of broken bonds (Fig. 12b). The curves “R6-RATIO-1.4%”, “R6-RATIO-2.18%” and “R6-RATIO-3.14%” represent reinforcement ratios equal to 1.4%, 2.18% and 3.14% of the total volumes of the reinforced concrete members, respectively. It is worth noting that the reinforcement ratio is increased, considering the same volume of the reinforcement bar and reducing the volume of concrete. The effect of reinforcement ratio is investigated by using particles with the radius equal to 0.6 mm. The load displacement curve, representing the lowest concrete volume and the highest reinforcement ratio equal to 3.14% of the volume, is located below other curves, which corresponds to higher values of displacements (Fig. 12a) and significantly larger percentage of the broken bonds (Fig. 12b).

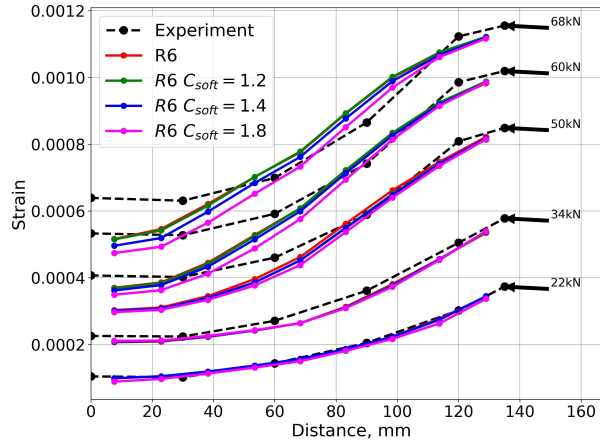


FIG. 13. Strain dependency on the distance from specimen centre for different loads in case of the elastic-softening constitutive model.

Figure 13 illustrates the application of the elastic-softening constitutive model. The dependency of the strain on the distance from specimen centre is investigated in the case of different softening slopes. It is assumed that values of the softening parameters $c_n^{soft} = c_t^{soft} = c^{soft}$ are the same in the normal direction and in the tangential direction. A set of curves “Experiment” represents the reinforcement strain profiles obtained from experimental measurements for different load values. The set of curves “R6” represents the strain profiles computed numerically by using 627264 particles in the case of the elastic perfectly brittle constitutive model. The sets of curves “R6 $C_{soft} = 1.2$ ”, “R6 $C_{soft} = 1.4$ ” and “R6 $C_{soft} = 1.8$ ” represent the strain profiles computed numerically by using the elastic-softening constitutive model with the softening parameter equal to 1.2, 1.4 and 1.8, respectively. It can be observed that increased values of the softening parameter decrease the strain values at the midsection of the specimen in case of the large load values. In general, the introduced softening leads to existence of tension forces between particles after bond breakage, which reduces the strain values in the specimen. However, the obtained curves show that the influence of the softening is not significant. Moreover, the employed elastic-softening constitutive model does not lead to better agreement of the numerical solution with the experimental measurements.

7. Conclusions

The newly developed GPU-based DEM code is applied to simulate brittle damage of reinforced concrete and to investigate the discretization scale of the

reinforcement bar geometry, which requires millions of particles. The computational performance of the developed GPU code and applicability of the DEM methodology is examined, simulating the double pull-out test of the short reinforced concrete member. The contribution of the reinforcement bar geometry, considering ribs, and its discretisation issues are investigated by using three samples with radii of particles equal to 0.8 mm, 0.6 mm and 0.5 mm that yield sets of 377844, 627264 and 1089892 particles, respectively. Thus, the relatively small refinement reveals dramatic increase of the number of particles, which illustrates the complexity of the discretisation problem.

Qualitatively, contribution of refinement is demonstrated by the shape of cracking patterns, where regular propagation of radial cracks and born of longitudinal crack is observed. The visual comparison of longitudinal crack on the end of the specimen shows adequacy with the experiment. Quantitatively, the contribution of the refinement is evaluated by the difference between numerically calculated and experimentally measured values of the reinforcement strain profile and the load-displacement relationship, where convergence of modelling results to experiment is observed. As expected, higher accuracy of strains is achieved by using a larger number of particles. In the case of the largest number of particles equal to 1089892 (radius $R = 0.5$ mm), the averaged numerical error varies from 3.0% to 9.1% of the experimentally measured strain for different load values. In the case of the reference model with 627264 (radius $R = 0.6$ mm) particles, only insignificant changes can be observed that lead to variation of the averaged difference from 3.1% to 10.5% of the experimentally measured strain. However, in the case of the rough discretization, containing 377844 particles (radius $R = 0.8$ mm), the averaged difference varies from 4.2% to 14.9% of the experimentally measured strain for different loads. The application of the elastic-softening constitutive model with the softening parameter equal to 1.8 leads to increase of the averaged difference, which varies from 5.0% to 13.6% of the experimentally measured strain in the case of the reference model. The obtained results help to understand the contribution of discretization scale of the ribs to cracking patterns.

The developed GPU algorithm does not require any atomic operation for efficient handling of computations on bonds between particles, but the size of additional data arrays is increased, which requires the efficient memory management. The Cundall number equal to $4.3E+07$ is obtained on NVIDIA®Tesla™P100 GPU in the case of 1858560 particles, which demonstrates high performance of the code based on the implementation of the complex physical model. The same OpenCL code optimized for shared memory architectures is executed on different CPUs to evaluate the speed-up ratio of GPU to CPU. Sufficiently high speed-up values, varying from 2.71 to 9.58, are observed for different CPUs and different numbers of particles. Thus, the developed GPU code efficiently handles millions

of discrete particles necessary for damage and fracture simulations of reinforced concrete.

Acknowledgements

The present research is part of the project No. 09.3.3-LMT-K-712-02-0131, funded under the European Social Fund measure „Strengthening the Skills and Capacities of Public Sector Researchers for Engaging in High Level R&D Activities”, administered by the Research Council of Lithuania.

References

1. P.A. CUNDALL, O.D.L. STRACK, *A discrete numerical model for granular assemblies*, Géotechnique, **29**, 1, 47–65, 1979.
2. A. DŽIUGYS, B. PETERS, *An approach to simulate the motion of spherical and non-spherical fuel particles in combustion chambers*, Granular Matter, **3**, 4, 231–266, 2001.
3. H.P. ZHU, Z.Y. ZHOU, R.Y. YANG, A.B. YU, *Discrete particle simulation of particulate systems: Theoretical developments*, Chemical Engineering Science, **62**, 13, 3378–3396, 2007.
4. C.J. COETZEE, *Review: Calibration of the discrete element method*, Powder Technology, **310**, 104–142, 2017.
5. N. GOVENDER, D.N. WILKE, C.-Y. WU, J. KHINAST, P. PIZETTE, W. XU, *Hopper flow of irregularly shaped particles (non-convex polyhedra): GPU-based DEM simulation and experimental validation*, Chemical Engineering Science, **188**, 34–51, 2018.
6. A. KAČENIAUSKAS, R. KAČIANAUSKAS, A. MAKNICKAS, D. MARKAUSKAS, *Computation and visualization of discrete particle systems on gLite-based grid*, Advances in Engineering Software, **42**, 5, 237–246, 2011.
7. R. TYKHONIUK, J. TOMAS, S. LUDING, M. KAPPL, L. HEIM, H.J. BUTT, *Ultrafine cohesive powders: From interparticle contacts to continuum behaviour*, Chemical Engineering Science, **62**, 11, 2843–2864, 2007.
8. S. WANG, K. LUO, S. YANG, C. HU, J. FAN, *Parallel LES-DEM simulation of dense flows in fluidized beds*, Applied Thermal Engineering, **111**, 1523–1535, 2017.
9. J. ROJEK, E. OÑATE, C. LABRA, H. KARGL, *Discrete element simulation of rock cutting*, International Journal of Rock Mechanics and Mining Sciences, **48**, 6, 996–1010, 2011.
10. B. KRAVETS, H. KRUGGEL-EMDEN, *Investigation of local heat transfer in random particle packings by a fully resolved LBM-approach*, Powder Technology, **318**, 293–305, 2017.
11. R. KAČIANAUSKAS, A. MAKNICKAS, D. VAINORIUS, *DEM analysis of acoustic wake agglomeration for mono-sized microparticles in the presence of gravitational effects*, Granular Matter, **19**, 3, 48–60, 2017.
12. R. KAČIANAUSKAS, V. RIMŠA, A. KAČENIAUSKAS, A. MAKNICKAS, D. VAINORIUS, R. PACEVIČ, *Comparative DEM-CFD study of binary interaction and acoustic agglomeration of aerosol microparticles at low frequencies*, Chemical Engineering Research and Design, **136**, 548–563, 2018.

13. S. HENTZ, L. DAUDEVILLE, F.V. DONZÉ, *Identification and Validation of a discrete element model for concrete*, Journal of Engineering Mechanics, **130**, 6, 709–719, 2004.
14. G. LILLIU, J.G. MIER, *3D lattice type fracture model for concrete*, Engineering Fracture Mechanics, **70**, 927–41, 2003.
15. M. OSTOJA-STARZEWSKI, *Lattice models in micromechanics*, Lattice models in micromechanics, **55**, 35–61, 2002.
16. G.A. D’ADDETTA, F. KUN, E. RAMM, *On the application of a discrete model to the fracture process of cohesive granular materials*, Granular Matter, **4**, 77–90, 2002.
17. M. NITKA, J. TEJCHMAN, *A three-dimensional meso-scale approach to concrete fracture based on combined DEM with X-ray MCT images*, Cement and Concrete Research, **107**, 11–29, 2018.
18. D.O. POTYONDY, P.A. CUNDALL, *A bonded-particle model for rock*, International Journal of Rock Mechanics and Mining Sciences, **41**, 8, 1329–1364, 2004.
19. G. CUSATIS, D. PELESSONE, A. MENCARELLI, *Lattice Discrete Particle Model (LDPM) for failure behavior of concrete*, Cement and Concrete Composites, **33**, 881–971, 2011.
20. E. LALE, R. REZAKHANI, M. ALNAGGAR, G. CUSATIS, *Homogenization coarse graining (HCG) of the lattice discrete particle model (LDPM) for the analysis of reinforced concrete structures*, Engineering Fracture Mechanics, **197**, 259–336, 2018.
21. X. LIANG, C. WU, *Meso-scale modelling of steel fibre reinforced concrete with high strength*, Construction and Building Materials, **165**, 187–285, 2018.
22. J. ZHANG, Z. WANG, H. YANG, Z. WANG, X. SHU, *3D meso-scale modeling of reinforcement concrete with high volume fraction of randomly distributed aggregates*, Construction and Building Materials, **164**, 350–61, 2018.
23. J. REN, Z. TIAN, J. BU, *Simulating tensile and compressive failure process of concrete with a user-defined bonded-particle model*, International Journal of Concrete Structures and Materials, **12**, 1, 56–74, 2018.
24. D. ZABULIONIS, O. LUKOŠEVIČIENČ, R. KAČIANAUSKAS, L. TUMONIS, R. KLIUKAS, *Stochastic lattice modelling of the force-displacement and cracking behaviour of the steel reinforced tie*, Mathematical Problems in Engineering, **2019**, 1–17, 2019.
25. T. RABCZUK, G. ZI, S. BORDAS, H. NGUYEN-XUAN, *A geometrically non-linear three-dimensional cohesive crack method for reinforced concrete structures*, Engineering Fracture Mechanics, **75**, 4740–4808, 2008.
26. T. RABCZUK, T. BELYTSCHKO, *Application of particle methods to static fracture of reinforced concrete structures*, International Journal of Fracture, **137**, 19–49, 2006.
27. P. DESNERCK, J.M. LEES, C.T. MORLEY, *Bond behaviour of reinforcing bars in cracked concrete*, Construction and Building Materials, **94**, 126–172, 2015.
28. D. MARKAUSKAS, A. KAČENIAUSKAS, *The comparison of two domain repartitioning methods used for parallel discrete element computations of the hopper discharge*, Advances in Engineering Software, **84**, 68–76, 2015.
29. A. KAČENIAUSKAS, R. PACEVIČ, V. STARIKOVIČIUS, A. MAKNICKAS, M. STAŠKŪNIENČ, G. DAVIDAVIČIUS, *Development of cloud services for patient-specific simulations of blood flows through aortic valves*, Advances in Engineering Software, **103**, 57–64, 2017.

-
30. A. KAČENIAUSKAS, P. RUTSCHMANN, *Parallel FEM software for CFD problems*, Informatica, **15**, 3, 363–378, 2004.
 31. NVIDIA, *Compute unified device architecture*, 2018, <https://docs.nvidia.com/cuda/>.
 32. J.E. STONE, D. GOHARA, G. SHI, *OpenCL: A parallel programming standard for heterogeneous computing systems*, Computing in Science & Engineering, **12**, 3, 66–73, 2010.
 33. C.A. RADEKE, B.J. GLASSER, J.G. KHINAST, *Large-scale powder mixer simulations using massively parallel GPU architectures*, Chemical Engineering Science, **65**, 24, 6435–6442, 2010.
 34. D. NISHIURA, M. FURUICHI, H. SAKAGUCHI, *Computational performance of a smoothed particle hydrodynamics simulation for shared-memory parallel computing*, Computer Physics Communications, **194**, 18–32, 2015.
 35. X. YUE, H. ZHANG, C. KE, C. LUO, S. SHU, Y. TAN, C. FENG, *A GPU-based discrete element modeling code and its application in die filling*, Computers & Fluids, **110**, 235–244, 2015.
 36. Z. ZHENG, M. ZANG, S. CHEN, H. ZENG, *A GPU-based DEM-FEM computational framework for tire-sand interaction simulations*, Computers & Structures, **209**, 74–92, 2018.
 37. T. WASHIZAWA, Y. NAKAHARA, *Parallel Computing of discrete element method on GPU*, Applied Mathematics, **4**, 1, 242–247, 2013.
 38. Y. TIAN, S. ZHANG, P. LIN, Q. YANG, G. YANG, L. YANG, *Implementing discrete element method for large-scale simulation of particles on multiple GPUs*, Computers & Chemical Engineering, **104**, 231–240, 2017.
 39. J.Q. GAN, Z.Y. ZHOU, A.B. YU, *A GPU-based DEM approach for modelling of particulate systems*, Powder Technology, **301**, 1172–1182, 2016.
 40. J. ZHENG, X. AN, M. HUANG, *GPU-based parallel algorithm for particle contact detection and its application in self-compacting concrete flow simulations*, Computers & Structures, **112–113**, 193–204, 2012.
 41. M. DURAND, P. MARIN, F. FAURE, B. RAFFIN, *DEM-based simulation of concrete structures on GPU*, European Journal of Environmental and Civil Engineering, **16**, 9, 1102–1114, 2012.
 42. E.M.B. CAMPELLO, *A description of rotations for DEM models of particle systems*, Computational Particle Mechanics, **2**, 109–134, 2015.
 43. L. TUMONIS, R. KAČIANAUSKAS, A. KAČENIAUSKAS, *Evaluation of friction due to deformed behaviour of rail in the electromagnetic railgun: numerical investigation*, Mechanika, **63**, 1, 58–63, 2007.
 44. E. STUPAK, R. KAČIANAUSKAS, A. KAČENIAUSKAS, V. STARIKOVIČIUS, A. MAKNICKAS, R. PACEVIČ, M. STAŠKŪNIENČ, G. DAVIDAVIČIUS, A. AIDIETIS, *The geometric model-based patient-specific simulations of turbulent aortic valve flows*, Archives of Mechanics, **69**, 4–5, 317–345, 2017.
 45. G. LIU, J.S. MARSHALL, S.Q. LI, Q. YAO, *Discrete-element method for particle capture by a body in an electrostatic field*, International Journal for Numerical Methods in Engineering, **84**, 13, 1589–1612, 2010.

46. A. ZANG, T.-F. WONG, *Elastic stiffness and stress concentration in cemented granular material*, International Journal of Rock Mechanics and Mining Sciences & Geomechanics Abstracts, **32**, 563–637, 1995.
47. S. PILKAVIČIUS, R. KAČIANAUSKAS, A. NORKUS, *Investigation of normal contact interaction between two bonded spherical particles*, Mechanika, **18**, 632–641, 2013.
48. D. ESTAY, F. CHACANA, J. IBARRA, L. PÉREZ, S. LASCANO, *Bond calibration method for Young's modulus determination in the discrete element method framework*, Granular Matter, **19**, 3, 60–67, 2017.
49. G.A. KOHRING, *Studies of diffusional mixing in rotating drums via computer simulations*, Journal de Physique I, **5**, 1551–1612, 1995.
50. H. KRUGGEL-EMDEN, S. WIRTZ, V. SCHERER, *A study on tangential force laws applicable to the discrete element method (DEM) for materials with viscoelastic or plastic behavior*, Chemical Engineering Science, **63**, 1523–1564, 2008.
51. R. KAČIANAUSKAS, A. MAKNICKAS, A. KAČENIAUSKAS, D. MARKAUSKAS, R. BALEVIČIUS, *Parallel discrete element simulation of poly-dispersed granular material*, Advances in Engineering Software, **41**, 1, 52–63, 2010.
52. R. PACEVIČ, A. KAČENIAUSKAS, *The development of VisLT visualization service in open-stack cloud infrastructure*, Advances in Engineering Software, **103**, 46–56, 2017.
53. G. KAKLAUSKAS, A. SOKOLOV, R. RAMANAUSKAS, R. JAKUBOVSKIS, *Reinforcement strains in reinforced concrete tensile members recorded by strain gauges and FBG sensors: experimental and numerical analysis*, Sensors, **19**, 200–213, 2019.
54. J. HOUDE, *Study of Force-Displacement Relationships for the Finite-Element Analysis of Reinforced Concrete*, Ph.D. Thesis, McGill University, Montreal, 1974.
55. R. JAKUBOVSKIS, G. KAKLAUSKAS, *Bond-stress and bar-strain profiles in RC tension members modelled via finite elements*, Engineering Structures, **194**, 138–146, 2019.

Received November 30, 2018; revised version September 20, 2019.

Published online October 25, 2019.
